

Heterostructured and Mesoporous Nb₂O₅@TiO₂ Core-Shell Spheres as Negative Electrode in Li-Ion Batteries

Wenlei Xu^a, Yaolin Xu^b, Thorsten Schultz^{cd}, Yan Lu^b, Norbert Koch^{cd}, Nicola Pinna^{a}*

^aInstitut für Chemie and IRIS Adlershof, Humboldt-Universität zu Berlin, Brook-Taylor-Str. 2, 12489 Berlin, Germany

^bDepartment of Electrochemical Energy Storage, Helmholtz-Zentrum Berlin für Materialien und Energie, 14109 Berlin, Germany

^cInstitut für Physik and IRIS Adlershof, Humboldt-Universität zu Berlin, Brook-Taylor-Str. 2, 12489 Berlin, Germany

^dHelmholtz-Zentrum Berlin für Materialien und Energie GmbH, 12489 Berlin, Germany

*E-mail: nicola.pinna@hu-berlin.de

Keywords: Nb₂O₅@TiO₂, mesoporous, heterostructures, core-shell spheres, lithium-ion batteries

ABSTRACT: Niobium pentoxides have received considerable attention and are promising anode materials for lithium-ion batteries (LIBs), due to their fast Li storage kinetics and high capacity. However, their cycling stability and rate performance are still limited owing to the intrinsic insulating properties and structural degradation during charging and discharging. Herein, a series of mesoporous Nb₂O₅@TiO₂ core-shell spherical heterostructures have been prepared for the first time by a sol-gel method and investigated as anode materials in LIBs. The mesoporosity can provide numerous open and short pathways for Li⁺ diffusion, meanwhile, heterostructures can simultaneously enhance the electronic conductivity, and thus improve the rate capability. The TiO₂ coating layer shows robust crystalline skeletons during repeated lithium insertion and extraction processes, retaining high structural integrity and, thereby, enhancing cycling stability. The electrochemical behavior is strongly dependent on the thickness of the TiO₂ layer. After optimization, a mesoporous Nb₂O₅@TiO₂ core-shell structure with a ~13 nm thick TiO₂ layer delivers a high specific capacity of 136 mAh g⁻¹ at 5 A g⁻¹, and exceptional cycling stability (88.3% retention over 1000 cycles at 0.5 A g⁻¹). This work provides a facile strategy to obtain mesoporous Nb₂O₅@TiO₂ core-shell spherical structures and underlines the importance of structural engineering for improving the performance of battery materials.

1. INTRODUCTION

To meet the growing demand for next-generation energy storage devices, many efforts have been made to explore alternative electrode materials with high capacity and long-term cycling stability for advanced lithium-ion batteries (LIBs).¹⁻³ Recently, Nb₂O₅ has been considered as a promising anode material due to its fast Li-(de)intercalation kinetics, promising capacity, and safe working potential (>1 V vs. Li⁺/Li).⁴⁻⁶ Among the different crystal structures of Nb₂O₅, the orthorhombic phase (T-Nb₂O₅) is the most suitable phase for LIBs, owing to its unique alternating dense-loose atomic packing arrangement, which offers low steric hindrance transport for Li-ions, and thus leads to fast Li-ion storage.⁷⁻⁹ Nb₂O₅ anodes with various nanostructures, such as nanosheets,^{10, 11} nanorods,¹² nanowires,^{13, 14} nanobelts,¹⁵ nanofibers,¹⁶ nanoparticles,¹⁷ and others, have been studied and achieve high-performance lithium storage. Moreover, Nb₂O₅ coated with various carbon materials has been reported and exhibits outstanding electrochemical behavior.^{5, 18-21}

It is notable that the large surface area of nanomaterials plays a major role in improving the electrolyte infiltration and shortening the Li-ion diffusion in the solid active material particles and thus facilitating the interfacial adsorption and the interfacial Faradaic reactions in the batteries, leading to enhanced capacity.²² However, it inevitably results in more severe side reactions, such as decomposition of the electrolyte, which leads to additional SEI formation.^{23, 24} Alternatively, developing micro-scale electrode materials, which are generally synthesized by solid-state reactions, has been widely studied in recent years. For example, Li's group reported that N-C@MSC-Nb₂O₅ achieved a high reversible capacity of 170 mAh g⁻¹ at 2.0 A g⁻¹ after 1000 cycles.²⁵ Grey's group demonstrated that micrometer-sized particles of bronze-phase Nb₂O₅ exhibited remarkable rate capability.⁹ In addition, porous materials have attracted extensive interest as they can provide large surface areas and a large number of pathways for fast Li-ion diffusion, and thus improve the electrochemical performance.²⁶⁻²⁸ Therefore, porous Nb₂O₅ with various structures has been widely investigated. Previous work demonstrated that mesoporous T-Nb₂O₅ nanofibers,^{16, 29} mesoporous T-Nb₂O₅ nanobelts,¹⁵ mesoporous Nb₂O₅/carbon composites,^{30, 31} partially single-crystalline mesoporous T-Nb₂O₅ nanosheets,³² and mesoporous Nb₂O₅ microspheres^{33, 34} could provide high specific capacity and rate performance. However, these porous Nb₂O₅ structures are usually made of interconnected nanoparticles, which have a large amount of grain boundaries and undergo severe structural degradation during long cycling.

Interestingly, it has been demonstrated that heterostructures can not only increase the electronic conductivity but also enhance the structural integrity.³⁵⁻⁴¹ Consequently, improved electrochemical properties of heterostructured electrode materials can be expected. Creating heterostructures with carbon materials has been considered as an effective way to improve the rate capability and cycling stability.^{5, 16, 17, 30, 31, 33, 42} However, this approach still suffers from some drawbacks. These additives or conductive layers just alter the electron transfer on the external layer or at the interface of the neighboring active materials, instead of improving the intrinsically poor conductivity of the inner core.⁴³ Besides, the low density of carbon will cause low packing efficiency of the electrode materials and thus result in low volumetric capacity, which limit their practical application.^{25, 44} Nevertheless, heterostructures, formed by coupling nanocrystals with different band gaps, can establish an internal electric field at the interface, which will facilitate charge transfer and enhance the reaction kinetics.^{37, 39, 40, 45, 46} It is well known that TiO₂ shows low strain properties upon lithiation, and the lithiated TiO₂ can increase the electrical conductivity of

the electrode.^{38,48} Therefore, TiO₂ with anatase and rutile phases have been reported as promising and effective encapsulating layers to create core-shell heterostructures.^{38, 48-51}

Compared to heterostructuring, the utilization of mixed oxides such as titanium niobium oxide, which has a crystallographic shear structure with 3×3 blocks of MO₆ (M = Ti, Nb) octahedra, is also an effective method to improve the structural stability and long-term cyclability of Nb₂O₅ upon repetitive de-/intercalation of Li-ions, as these blocks are connected by sharing edges and bounded by crystallographic shear planes, guaranteeing a high structural stability and providing numerous vacant sites for Li-ion insertion.⁵⁰ For example, Guo's group prepared 2D nanoporous TiNb₂O₇ with a sol-gel method, delivering long-term cyclability (200 mAh g⁻¹ after 1000 cycles at 5 C).⁵² Chen's group reported that Ti₂Nb₁₀O₂₉ exhibited the similar crystal structure as TiNb₂O₇, and achieved a high reversible capacity of 144 mAh g⁻¹ at 10 C after 800 cycles.⁵³ However, pure titanium niobium oxides exhibit a low Li-ion diffusion coefficient and poor electronic conductivity, which is attributed to the empty 3d/4d orbitals in the Ti/Nb metal d-band,⁵⁴ limiting the fast-charging capability of batteries.

In this work, we designed and fabricated mesoporous Nb₂O₅@TiO₂ core-shell spherical heterostructures with various shell thicknesses via a facile and reproducible sol-gel method, in which Nb₂O₅ spheres act as the core and TiO₂ is the shell layer. This strategy allows us to control the composition, morphology, and thickness of the coating layer, and to tailor the electrochemical behavior of the heterostructured materials. Though there have been reports of heterostructures between Nb₂O₅ and TiO₂ for LIBs,⁵⁵⁻⁵⁷ the novel non-hydrolytic sol-gel synthesis developed in this work allows for precisely controlling the morphology of mesoporous Nb₂O₅ spheres. Meanwhile, Nb₂O₅@TiO₂ core-shell heterostructures with various controlled shell crystallinity and thicknesses are successfully synthesized for the first time, allowing for comprehending in detail the role of the TiO₂ shell in the core-shell heterostructures during de-/lithiation of the Nb₂O₅ core. Owing to the synergistic effects of mesoporous Nb₂O₅, which provides a high specific capacity, and TiO₂, which can help to maintain the structural integrity, the optimized mesoporous Nb₂O₅@TiO₂ core-shell spheres exhibit excellent rate capability and long-term cycling lifetime which is superior to Nb₂O₅ and TiO₂ alone.

2. RESULTS AND DISCUSSION

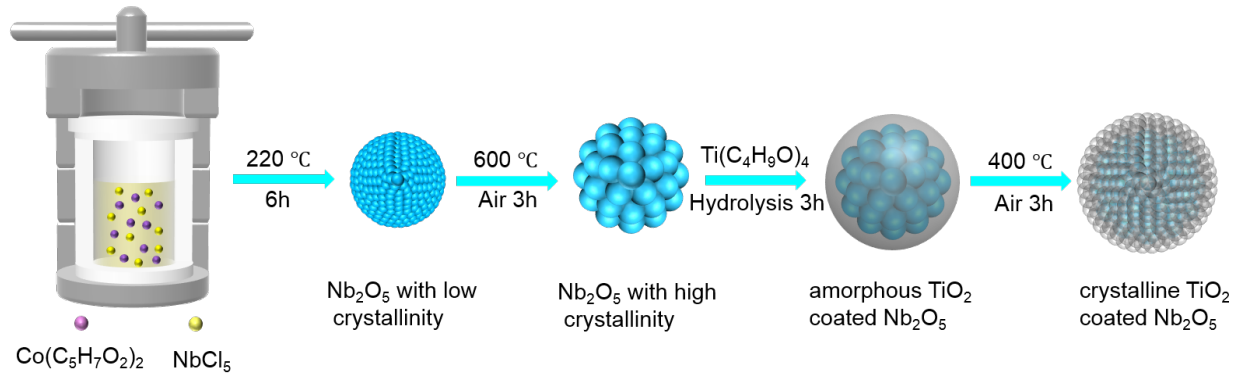


Figure 1. Schematic illustration of the formation of Nb_2O_5 and $\text{Nb}_2\text{O}_5@\text{TiO}_2$.

The synthesis of $\text{Nb}_2\text{O}_5@\text{TiO}_2$ core-shell spherical heterostructures is schematically depicted in **Figure 1**. First, Nb_2O_5 spherical structures with low crystallinity are formed by aldol condensation reaction of acetophenone in the presence of Co^{2+} ions, catalyzed by the NbCl_5 (Lewis acid). The proposed reaction mechanism has been reported in our previous work.^{5, 58} The cobalt additive only acts as a promoter for the self-assembly of the nanocrystals,⁵⁹ and was not detected in the final products by energy dispersive X-ray spectroscopy (EDX) and X-ray photoelectron spectroscopy (XPS) characterization (**Figure S1**). Then, a thermal treatment was applied to obtain Nb_2O_5 with high crystallinity. Afterwards, amorphous TiO_2 shells are uniformly deposited on the surface of Nb_2O_5 spheres via a sol-gel coating method ($\text{Nb}_2\text{O}_5@\text{TiO}_2\text{a-X}$, where X is the thickness of the TiO_2 shell in nm). Finally, $\text{Nb}_2\text{O}_5@\text{TiO}_2\text{a-X}$ is thermally treated at 400 °C under air to crystallize the TiO_2 shell ($\text{Nb}_2\text{O}_5@\text{TiO}_2\text{c-X}$ where X is the thickness of the TiO_2 shell in nm). In addition, TiO_2 nanoparticles are fabricated directly by sol-gel processes and then calcinated in air.

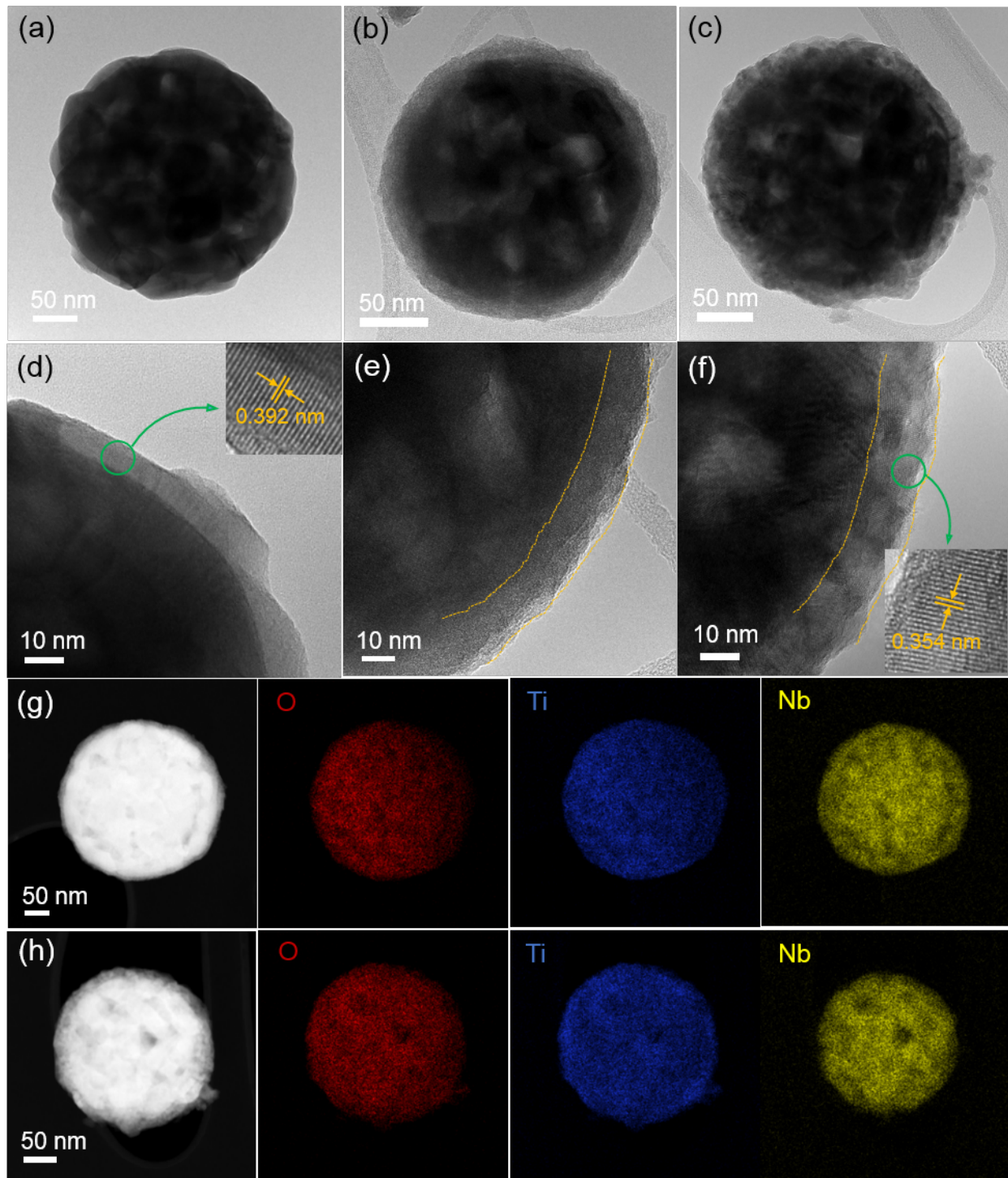


Figure 2. TEM images of (a, d) Nb_2O_5 , (b, e) $\text{Nb}_2\text{O}_5@\text{TiO}_2\text{a-14}$, and (c, f) $\text{Nb}_2\text{O}_5@\text{TiO}_2\text{c-13}$. STEM-HAADF images and the corresponding EDX elemental mappings of (g) $\text{Nb}_2\text{O}_5@\text{TiO}_2\text{a-14}$, and (h) $\text{Nb}_2\text{O}_5@\text{TiO}_2\text{c-13}$.

The morphology and microstructure of the composites were characterized by scanning electron microscopy (SEM) and transmission electron microscopy (TEM). As shown in **Figure S2a** and **2a**, Nb_2O_5 exhibits spherical morphology with a rough surface, and the spherical diameters are in the range of 200-400 nm. The rough surface of the Nb_2O_5 spheres can provide high energy nucleation sites for the tight growth of TiO_2 during the synthesis process.⁴³ After being coated with a TiO_2 layer, the spherical morphology stays unchanged, and Nb_2O_5 spheres are uniformly encapsulated by the TiO_2 layers (**Figure S2b**, **S2c**, **2b**, and **2c**). Such a structure can prevent the structural collapse of the Nb_2O_5 spheres caused by Li^+ insertion, enhancing its structural stability.^{46, 47, 49} For comparison, TiO_2 was prepared using the same sol-gel method without the addition of Nb_2O_5 spheres, leading to agglomerated nanoparticles (**Figure S2d**, **S3a**). High-resolution TEM images and selected area electron diffraction (SAED) patterns (**Figure 2d**, **S3b-f**) demonstrate the polycrystalline nature of Nb_2O_5 and TiO_2 , and match well with the orthorhombic Nb_2O_5 ($\text{T-Nb}_2\text{O}_5$) and tetragonal anatase TiO_2 phases. The lattice fringes with an interlayer spacing of 0.392 nm can be assigned to the (001) plane of $\text{T-Nb}_2\text{O}_5$. Meanwhile, the plane spacing of 0.354 nm matches well with the (101) plane of anatase TiO_2 . The HRTEM image and SAED pattern of $\text{Nb}_2\text{O}_5@\text{TiO}_2\text{a-14}$ (**Figure 2e**, **S3e**) reveals the amorphous nature of the TiO_2 layer, as no lattice fringes or diffraction rings can be observed. The maximum and minimum thicknesses of amorphous TiO_2 layer are 20.4 nm and 6.3 nm, respectively, and the average thickness is about 14 nm (**Figure S4a**). After thermal treatment, the amorphous TiO_2 layer is converted into a crystalline structure (**Figure 2f**). The maximum and minimum thicknesses of anatase TiO_2 layer are 20.7 nm and 4.3 nm, respectively, with an average thickness of about 13 nm (**Figure S4b**). Moreover, the coexistence of diffraction rings of Nb_2O_5 and TiO_2 in the corresponding SAED pattern (**Figure S3f**) confirms the formation of a crystalline $\text{Nb}_2\text{O}_5@\text{TiO}_2$ heterostructure. The scanning transmission electron microscopy images, using a high-angle annular dark-field detector (HAADF-STEM), of a single $\text{Nb}_2\text{O}_5@\text{TiO}_2\text{a-14}$ or $\text{Nb}_2\text{O}_5@\text{TiO}_2\text{c-13}$ sphere, combined with the corresponding elemental mappings for O, Ti, and Nb, demonstrate a well-defined core-shell structure with a homogeneous TiO_2 layer onto the Nb_2O_5 sphere (**Figure 2g**, **2h**).

To study the specific surface areas and pore size distributions of the composites, nitrogen adsorption-desorption experiments were performed and the results are presented in **Figure S5**. All the samples display a typical type IV isotherm, which is characteristic of mesoporous materials.

Moreover, TiO_2 exhibits a sharp capillary condensation step in the high pressure region, due to the aggregated nanoparticles structure,⁴⁷ which has been demonstrated by SEM and TEM analysis (**Figure S2d, S3a**). The Brunauer-Emmett-Teller (BET) specific surface areas of TiO_2 , Nb_2O_5 , $\text{Nb}_2\text{O}_5@\text{TiO}_2\text{a-14}$, and $\text{Nb}_2\text{O}_5@\text{TiO}_2\text{c-13}$ are 15, 21, 73, 33 $\text{m}^2 \text{ g}^{-1}$, respectively. Nb_2O_5 , $\text{Nb}_2\text{O}_5@\text{TiO}_2\text{a-14}$, and $\text{Nb}_2\text{O}_5@\text{TiO}_2\text{c-13}$ have mainly pores of size 23-30 nm. Noting that $\text{Nb}_2\text{O}_5@\text{TiO}_2\text{a-14}$ possesses larger specific surface areas than $\text{Nb}_2\text{O}_5@\text{TiO}_2\text{c-13}$, which could be ascribed to its poor crystallinity and the presence of numerous TiO_2 nanograins, leading to abundant small pores in between.⁴⁶ During annealing, the tiny nanograins tend to aggregate to minimize the total surface energy, resulting in a reduced specific surface area for $\text{Nb}_2\text{O}_5@\text{TiO}_2\text{c-13}$. TiO_2 nanoparticles alone tend to agglomerate and thus exhibit the smallest specific surface area.

The composition and crystal structure of the samples were analyzed by X-ray diffraction (XRD). As illustrated in **Figure 3a**, the XRD pattern of TiO_2 can be well indexed to tetragonal anatase (ICDD No. 084-1286), and the XRD pattern of Nb_2O_5 matches well with the orthorhombic Nb_2O_5 phase (ICDD No. 030-0873). The XRD pattern of $\text{Nb}_2\text{O}_5@\text{TiO}_2\text{c-13}$ includes all the reflections of TiO_2 , which are not present in that of $\text{Nb}_2\text{O}_5@\text{TiO}_2\text{a-14}$, further confirming the amorphous nature of TiO_2 in $\text{Nb}_2\text{O}_5@\text{TiO}_2\text{a-14}$ and its successful crystallization in $\text{Nb}_2\text{O}_5@\text{TiO}_2\text{c-13}$, in agreement with the TEM results. It is worth noting that no crystalline impurities are detected in all the samples. The structure of the samples is further studied by Raman spectroscopy (**Figure 3b**). The spectrum of TiO_2 is typical for crystalline anatase TiO_2 ,^{60, 61} with the same contributions also present in the spectrum of $\text{Nb}_2\text{O}_5@\text{TiO}_2\text{c-13}$. Nb_2O_5 and $\text{Nb}_2\text{O}_5@\text{TiO}_2\text{a-14}$ show characteristic Raman modes of orthorhombic Nb_2O_5 phase.^{5, 8} The absence of Raman bands corresponding to anatase TiO_2 in $\text{Nb}_2\text{O}_5@\text{TiO}_2\text{a-14}$ heterostructures further confirms that the TiO_2 layer is amorphous.

X-ray photoelectron spectroscopy (XPS) was conducted to evaluate the chemical compositions and chemical states of the composites. The Nb_2O_5 sample (**Figure S1b**) only contains O and Nb (besides C and a small amount of Si from the carbon tape). The Nb 3d spectrum (**Figure 3c**) exhibits two peaks centered at 207.7 and 210.4 eV assigned to Nb 3d_{5/2} and Nb 3d_{3/2}, indicating the presence of Nb⁵⁺ in Nb_2O_5 .⁴⁵ **Figure S6a** shows that only O and Ti are present in the anatase TiO_2 sample. The Ti 2p core level of TiO_2 (**Figure 3d**) exhibits symmetrical Ti

2p doublets from Ti⁴⁺ ions.⁶² In Nb₂O₅@TiO₂a-14 and Nb₂O₅@TiO₂c-13, O, Ti, and Nb can be observed in the survey spectra (**Figure S6b**). Noticeably, compared to the pristine anatase TiO₂, the binding energies (BEs) of Ti 2p in Nb₂O₅@TiO₂a-14 and Nb₂O₅@TiO₂c-13 shift to higher BE, while the Nb 3d BEs of Nb₂O₅@TiO₂a-14 and Nb₂O₅@TiO₂c-13 shift to lower values in comparison with those of Nb₂O₅, suggesting an interface interaction caused by an electron transfer from TiO₂ to Nb₂O₅, resulting in an enhanced ionic and electronic conductivity due to the internal electric field at the heterointerfaces.^{37, 39, 45, 63} The XPS survey spectra of Nb₂O₅@TiO₂a-14 and Nb₂O₅@TiO₂c-13 show decreased intensity of Nb 3d peaks and a distinct peak of Ti 2p compared to pure Nb₂O₅ spheres, further confirming that the Nb₂O₅ cores are well encapsulated by the TiO₂ shells (**Figure S6b**), which is consistent with the SEM and TEM observations.

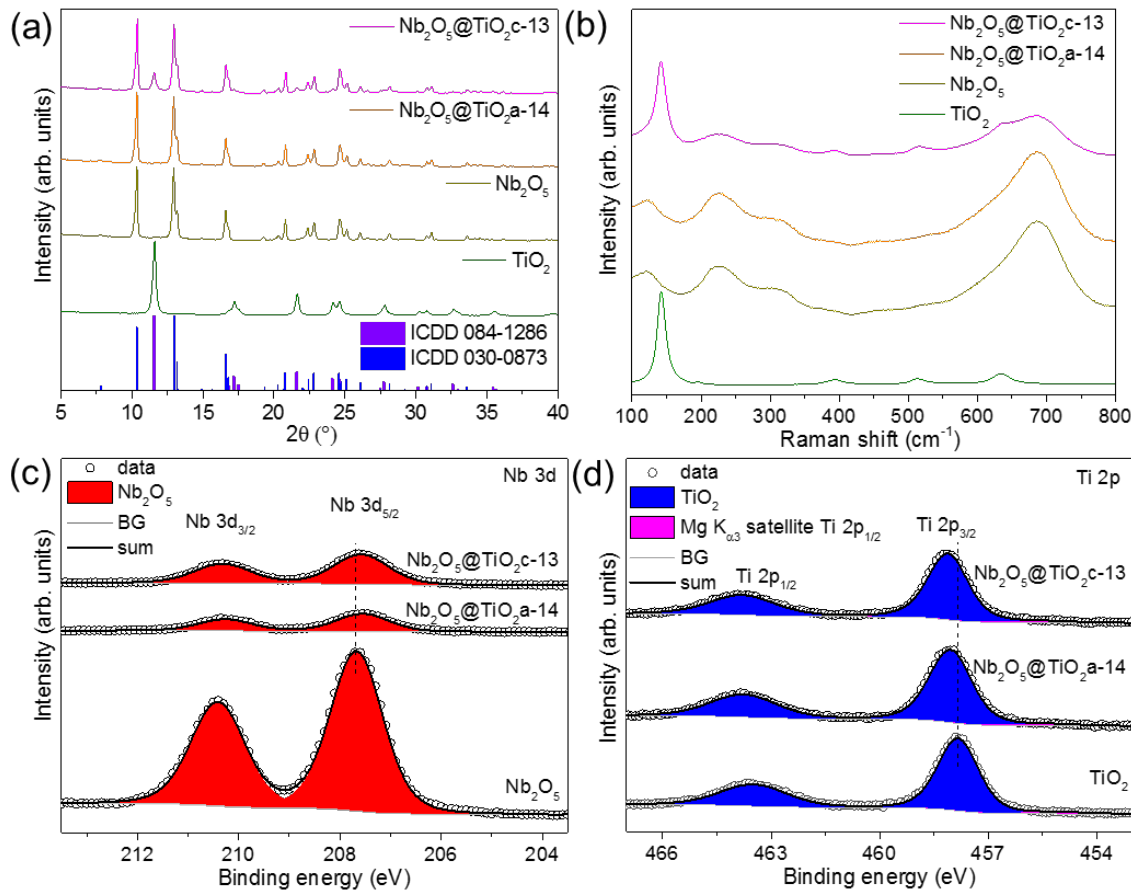


Figure 3. (a) XRD, (b) Raman, and (c, d) Nb 3d and Ti 2p XPS spectra of anatase TiO₂, Nb₂O₅, Nb₂O₅@TiO₂a-14, and Nb₂O₅@TiO₂c-13.

Based on the above discussion, we can confirm that the Nb₂O₅@TiO₂ core-shell sphere heterostructure has been successfully synthesized. In order to demonstrate the controllability of

the strategy and to find out the optimal synthesis parameters of the $\text{Nb}_2\text{O}_5@\text{TiO}_2$ core-shell sphere heterostructure for lithium-ion storage application, $\text{Nb}_2\text{O}_5@\text{TiO}_2$ core-shell spheres with different thicknesses of the crystalline TiO_2 layer (i.e. 5, 8, 13, and 22 nm) have been produced by modifying the concentration of the titanium precursor during the synthesis (TBOT, see experimental section). As shown in **Figure S7**, at low TBOT concentration, anatase TiO_2 shells can be deposited on the surface of Nb_2O_5 spheres, but not uniformly. With increasing the concentration of the TBOT, the homogeneity as well as the thickness of the anatase TiO_2 layer increase. **Table S1** shows the weight ratio between Nb_2O_5 and anatase TiO_2 . We further conducted XRD measurements for all these samples to evaluate their phases and purities. **Figure S8** shows that all the patterns can be indexed to the tetragonal anatase (ICDD No. 084-1286) and orthorhombic Nb_2O_5 (ICDD No. 030-0873), and no peaks for other impurities are observed, suggesting the coexistence of anatase TiO_2 and T- Nb_2O_5 , and the successful synthesis of $\text{Nb}_2\text{O}_5@\text{TiO}_2$ core-shell like heterostructures.

To optimize the thickness of the anatase TiO_2 layer for improved Li-ion storage performance, the $\text{Nb}_2\text{O}_5@\text{TiO}_2\text{c-5}$, $\text{Nb}_2\text{O}_5@\text{TiO}_2\text{c-8}$, $\text{Nb}_2\text{O}_5@\text{TiO}_2\text{c-13}$ and $\text{Nb}_2\text{O}_5@\text{TiO}_2\text{c-22}$ were electrochemically tested as electrode materials in LIBs. **Figure S9a** shows the rate capability of these composites at various current densities. As we can see, $\text{Nb}_2\text{O}_5@\text{TiO}_2\text{c-13}$ achieves larger capacities and superior rate capability over the other samples. When cycled at 0.1, 0.2, 0.5, 1, and 2 A g^{-1} , the $\text{Nb}_2\text{O}_5@\text{TiO}_2\text{c-13}$ electrode delivers reversible capacities of 206, 204, 192, 179, and 161 mAh g^{-1} , respectively. Even at 5 A g^{-1} , the capacity can still be maintained at 132 mAh g^{-1} , corresponding to a capacity retention of 64%, which is higher than that of $\text{Nb}_2\text{O}_5@\text{TiO}_2\text{c-5}$, $\text{Nb}_2\text{O}_5@\text{TiO}_2\text{c-8}$, and $\text{Nb}_2\text{O}_5@\text{TiO}_2\text{c-22}$ (47%, 55%, and 38%, respectively). Importantly, as the current density is reset to 0.1 A g^{-1} , 219 mAh g^{-1} can be recovered, indicating its excellent reversibility. The increase of capacity can be related to the electrochemical activation processes of the electrode materials, resulting in an improved accessibility of Li-ions in the inner part of the active materials, and more active sites available for Li-ion storage. Similar activation process has been reported in literature.⁶⁴⁻⁶⁶ Moreover, when these four electrodes are cycled at a current density of 0.5 A g^{-1} (**Figure S9b**), a high capacity retention ratio of 88.3% is obtained for $\text{Nb}_2\text{O}_5@\text{TiO}_2\text{c-13}$ after 1000 cycles, which is higher than that of $\text{Nb}_2\text{O}_5@\text{TiO}_2\text{c-5}$ (78%), $\text{Nb}_2\text{O}_5@\text{TiO}_2\text{c-8}$ (86.5%), and $\text{Nb}_2\text{O}_5@\text{TiO}_2\text{c-22}$ (85.2%). Post-mortem TEM results (**Figure S10**) demonstrate that the thin anatase TiO_2 (5 and 8 nm) layer cracks and peels off, whereas the core-shell structure can be retained with relatively thicker (13 and 22 nm) anatase TiO_2 layer after long-term cycling.

Electrochemical impedance spectroscopy (EIS) tests were carried out to investigate the electrochemical kinetics of $\text{Nb}_2\text{O}_5@\text{TiO}_2\text{c}$ electrodes with different thickness. As shown in **Figure S9c**, with increasing thickness of the anatase TiO_2 layer, the charge transfer resistance decreases, and $\text{Nb}_2\text{O}_5@\text{TiO}_2\text{c-13}$ exhibits the best charge transfer kinetics. This might be because a thinner anatase TiO_2 layer could not build an effective inner electric field at the heterointerface as it cannot cover the entire surface of the Nb_2O_5 nanocrystals. However, the excessively thick anatase TiO_2 layer result in significant increase of charge transfer resistance, owing to its poor intrinsic electronic conductivity.

To sum up, 13 nm anatase TiO_2 coating layer leads to the best rate capability and cycling stability. When the anatase TiO_2 layer is thinner, the coating layer is not homogeneous and/or not strong enough to tolerate volume variation of the Nb_2O_5 core, and hence, the anatase TiO_2 shell tends to crack and detach from the Nb_2O_5 core, resulting in poor structural stability (see also below). However, if the coating layer is too thick, although strong enough to withstand the volume changes during cycling, the capacity is severely compromised. This can be ascribed to the sluggish Li^+ diffusion kinetics in anatase TiO_2 that results in less-efficient lithiation of thick anatase TiO_2 layers, leading to compromised electronic conduction as compared to thin anatase TiO_2 .^{49, 64, 67}

The optimization of synthesis parameters is crucial to achieve a highly conformal and homogeneous $\text{Nb}_2\text{O}_5@\text{TiO}_2$ core-shell like heterostructures with outstanding electrochemical performance. However, how the heterostructure affects the electrochemical properties in LIBs is still unclear.

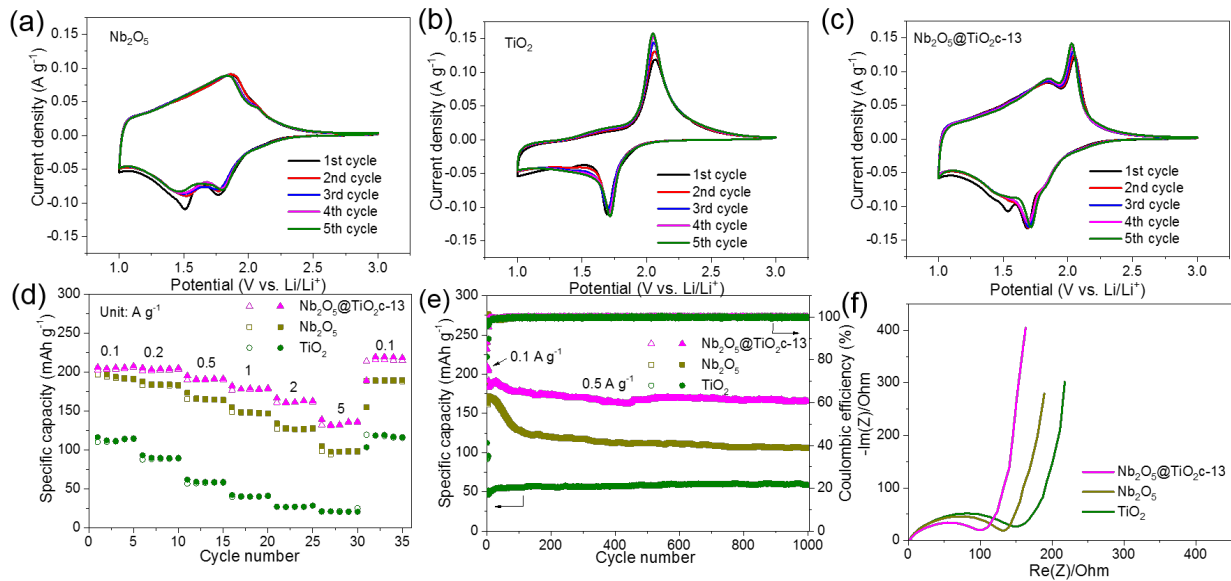


Figure 4. Electrochemical performances of Nb_2O_5 , anatase TiO_2 , and $\text{Nb}_2\text{O}_5@\text{TiO}_2\text{c-13}$ as anodes in Li-ion half cells. (a, b, c) CV curves at a scanning rate of 0.1 mV s^{-1} . (d) Rate performance. (e) Cycling performance at a current density of 0.5 A g^{-1} . Note that before cycling at 0.5 A g^{-1} , all the samples were dis-/charged for 5 cycles at 0.1 A g^{-1} . (f) EIS measurement.

To elucidate structure-electrochemical property relationships toward improvement of battery performance, various electrochemical measurements were carried out to investigate the Li-ion storage properties of the as-prepared $\text{Nb}_2\text{O}_5@\text{TiO}_2\text{c-13}$, Nb_2O_5 , and anatase TiO_2 as anode materials for LIBs. First, we conducted cyclic voltammogram (CV) measurements at a scan rate of 0.1 mV s^{-1} . **Figure 4a** shows the first five CV curves of the Nb_2O_5 electrode, the broad cathodic and anodic peaks are attributed to the reversible insertion/extraction of Li-ion in the niobium oxide structure. After the first cycle, the CV curves are nearly overlapping, suggesting a good reversibility and cycling stability of the lithium storage reactions. The Li-ion insertion/extraction reactions of Nb_2O_5 can be expressed as $\text{Nb}_2\text{O}_5 + x\text{Li}^+ + xe^- \leftrightarrow \text{Li}_x\text{Nb}_2\text{O}_5$, where x is the mole fraction of the inserted Li-ions which can be up to 2.^{5, 7} The distinct reduction peak at $\sim 1.71 \text{ V}$ and oxidation peak at $\sim 2.06 \text{ V}$ correspond to the typical lithiation and delithiation processes of anatase TiO_2 , respectively (**Figure 4b**).^{47, 64} Generally, the Li-ion insertion/extraction reactions of TiO_2 can be expressed as $\text{TiO}_2 + x\text{Li}^+ + xe^- \leftrightarrow \text{Li}_x\text{TiO}_2$, and the maximum capacity is $x = 1$. However, the maximum value of x is taken as 0.5 for the reversible reaction, due to the sluggish reaction kinetics at $x > 0.5$, corresponding to a capacity of 168 mAh g^{-1} .⁶⁸ It is noteworthy that the CV

curves of the $\text{Nb}_2\text{O}_5@\text{TiO}_2\text{c-13}$ electrode exhibit the combined features of Nb_2O_5 and anatase TiO_2 (**Figure 4c**).

Figure S11 shows the first two discharge-charge curves of Nb_2O_5 , anatase TiO_2 , and $\text{Nb}_2\text{O}_5@\text{TiO}_2\text{c-13}$ at 0.1 A g^{-1} . The initial discharge/charge capacities for $\text{Nb}_2\text{O}_5@\text{TiO}_2\text{c-13}$, Nb_2O_5 , and anatase TiO_2 anodes are $232.1/204.9$, $190.5/168.1$, and $112.4/91.6 \text{ mAh g}^{-1}$, corresponding to initial Coulombic efficiencies (CEs) of 88.3%, 88.2%, 81.5%, respectively. The initial capacity loss is probably due to the formation of solid electrolyte interphase (SEI) layer on the surface of electrodes as well as the sluggish kinetics of Li-ion diffusion in TiO_2 , especially during delithiation.^{67, 69} To compensate the initial capacity loss, several strategies have been reported to improve the CE, such as suppressing the SEI formation,⁷⁰ prelithiation,⁷¹ and creating an artificial SEI layer.⁷² In comparison, the achieved CEs are much higher compared to carbon-based anode materials (~50%),⁶⁶ benefiting from suppressed SEI formation due to their higher working voltages.

The rate performance of the samples was measured at various current densities ranging from 0.1 to 5 A g^{-1} (**Figure 4d**). Compared to Nb_2O_5 and anatase TiO_2 , the specific capacity of $\text{Nb}_2\text{O}_5@\text{TiO}_2\text{c-13}$ is substantially increased, especially at high current densities. At 0.1 A g^{-1} , the reversible specific capacities of Nb_2O_5 and anatase TiO_2 are 194 and 112 mAh g^{-1} , respectively, while at a high current density of 5 A g^{-1} , Nb_2O_5 and anatase TiO_2 can only deliver a capacity of 98 and 21 mAh g^{-1} , respectively. In contrast, the capacity retention of $\text{Nb}_2\text{O}_5@\text{TiO}_2\text{c-13}$ at 5 A g^{-1} is remarkably increased to 132 mAh g^{-1} , resulting from the improved electrochemical reaction kinetics benefiting from the heterostructure. Specially, the low capacity retention for anatase TiO_2 is rooted in its large particle size and agglomeration structure, which leads to sluggish kinetics for ion migration. The superiority of the core-shell $\text{Nb}_2\text{O}_5@\text{TiO}_2\text{c-13}$ heterostructures is also manifested by their prevailing cycling stability as shown in **Figure 4e** and **Figure S12**. 166 mAh g^{-1} is obtained for $\text{Nb}_2\text{O}_5@\text{TiO}_2\text{c-13}$ at 0.5 A g^{-1} after 1000 cycles, corresponding to a high capacity retention ratio of 88.3%, which is significantly higher than that of Nb_2O_5 (106 mAh g^{-1} , 62.3%), revealing its remarkable structural stability, which can be ascribed to the anatase TiO_2 layer and its low strain properties.^{38, 47, 50} Notably, anatase TiO_2 exhibits very low specific capacity of $\sim 60 \text{ mAh g}^{-1}$ despite its good cycling stability. The capacity increased gradually in the initial ~ 30 cycles, which could be attributed to the activation of the active materials for reversible electrochemical

de-/lithiation during battery operation. Furthermore, as shown in **Figure S13**, after cycling at 0.1 A g⁻¹ for 500 cycles, 195 mAh g⁻¹ can be obtained for Nb₂O₅@TiO_{2c}-13, with a capacity fade rate of 0.014% per cycle, while only 156 mAh g⁻¹ can be obtained for Nb₂O₅, demonstrating enhanced cycling stability, which could be due to the presence of anatase TiO₂ shell layer that can alleviate the mechanical stress generated in Nb₂O₅ and thus increase the structural integrity over cycling.

In addition, the electrochemical properties of Nb₂O₅@TiO_{2a}-14 has also been investigated to compare the influence of crystalline and amorphous forms of TiO₂ layer on Li-ion storage properties. As shown in **Figure S14**, the electrochemical performance of Nb₂O₅@TiO_{2c}-13 is superior to that of Nb₂O₅@TiO_{2a}-14, which might be due to the amorphous TiO₂'s lower electronic conductivity,⁷³ as well as lack of well-defined sites for Li-ion insertion due to its disordered atomic arrangement.⁷⁴ Moreover, it has been demonstrated that amorphous TiO₂ exhibits larger volume changes during repetitive de-/lithiation processes,⁷⁴ which aggravates the limited cycle life of Nb₂O₅@TiO_{2a}-14.

Finally, electrochemical impedance spectroscopy (EIS) tests were conducted to investigate the electrochemical kinetics of Nb₂O₅, anatase TiO₂, and Nb₂O₅@TiO_{2c}-13 electrodes. **Figure 4f** shows that all the Nyquist plots consist of a depressed semicircle in the high-to-medium frequency region and a straight line in the low-frequency region. The former is attributed to charge transfer resistance at the electrode/electrolyte interface, while the latter is related to the Warburg impedance, which depends on the solid-state diffusion of Li-ions in the bulk electrode material. The high-frequency intercept at the x-axis is the total resistance of the electrolyte, separator, and electrode.^{67, 75} Nb₂O₅@TiO_{2c}-13 has the lowest charge-transfer resistance, suggesting fast electrochemical reaction kinetics for Li⁺ insertion/extraction. Besides, Nb₂O₅@TiO_{2c}-13 exhibits the highest slope in the low-frequency region, indicating its rapid Li⁺ diffusion property.⁴⁰

In order to reveal the kinetics of Li-ion storage, **Figure S15** compares the CV curves of Nb₂O₅@TiO_{2c}-13, Nb₂O₅, and TiO₂ electrodes at scan rates of 0.1-1.0 mV s⁻¹. As the scan rate increases, the CV curves maintain similar shapes and redox peaks become stronger, meanwhile, a shift in peak position can be observed, suggesting a slight polarization phenomenon. Generally, The relationship between the current (*i*) and the sweep rates (*v*) follows the power law:⁷

$$i = a v^b \quad (1)$$

Where a and b are variable parameters and the b parameter can be obtained from the slope of the $\log(i)$ versus $\log(v)$ plot. In particular, $b=1$ represents the capacitive-dominated behavior, $b=0.5$ represents the diffusion-controlled process. As shown in **Figure S15b, d, and f**, all these b values are between 0.5 and 1.0, indicative of fast surface redox kinetics, which means the achieved capacities are mainly derived from capacitive-controlled pseudocapacitive reaction. In addition, the contribution of capacitive-controlled ($k_1 v$) and diffusion-controlled ($k_2 v^{0.5}$) processes can be further quantified according to:⁷⁶

$$i = k_1 v + k_2 v^{0.5} \quad (2)$$

Where v is the sweep rate, constants (k_1 and k_2) can be calculated from the plots of $i/v^{0.5}$ versus $v^{0.5}$ followed by linear regression. The results were concluded in **Figure S16**, with increasing the scan rate, the capacitive contribution of $\text{Nb}_2\text{O}_5@\text{TiO}_2\text{c-13}$ gradually increased from 84.9% to 94.7%, demonstrating that the capacitive-controlled process is dominant. Meanwhile, the capacitive contributions of Nb_2O_5 and TiO_2 exhibit a similar trend with the increasing scan rate but remarkably lower than those of $\text{Nb}_2\text{O}_5@\text{TiO}_2\text{c-13}$. This could be related to its larger specific surface area, facilitating fast kinetics of Li-ion insertion/extraction. Besides, the presence of the internal electric field at the heterointerfaces of Nb_2O_5 and TiO_2 also contribute to the pseudocapacitive reaction, as it can result in an enhanced ionic and electronic conductivity, and thus, increased rate capability of $\text{Nb}_2\text{O}_5@\text{TiO}_2\text{c-13}$.⁴⁵

Galvanostatic intermittent titration technique (GITT) analysis was further carried out to evaluate the Li-ion diffusion kinetics in $\text{Nb}_2\text{O}_5@\text{TiO}_2\text{c-13}$, Nb_2O_5 , and TiO_2 during de-/lithiation. **Figure S17a and b** show the GITT curves of these three samples. The Li-ion diffusion coefficient (D_0) can be estimated by using Fick's second law through the following equation:¹⁷

$$D_0 = \frac{4}{\pi\tau} \left(\frac{m_B V_M}{M_B S} \right)^2 \left(\frac{\Delta E_S}{\Delta E_\tau} \right)^2 (\tau \ll \frac{L^2}{D_0}) \quad (3)$$

Where V_M is the molar volume of the active material, M_B is the molecular mass of the active material, m_B is the mass of the active material in the electrode, L is the electrode thickness, S is the surface area of the electrode, τ is the duration of a current pulse, ΔE_S is the change in the equilibrium potential, and ΔE_τ is the change in potential after the pulse. The last two parameters can be obtained from the voltage profiles during the GITT test (**Figure S18**). As shown in **Figure S17c and d**, TiO_2 and Nb_2O_5 exhibit the lowest and highest D_0 values, respectively, during

lithiation, indicating that the Li-ion diffusion kinetics in TiO_2 is kinetically more sluggish and thus is the kinetic limiting factor of Li-ion diffusion in the heterostructure during the uptake of Li-ions. Different from the lithiation process, the diffusion coefficient of the $\text{Nb}_2\text{O}_5@\text{TiO}_2\text{c-13}$ heterostructure is higher than those of TiO_2 and Nb_2O_5 during delithiation, which could be caused by the enhanced ionic conductivity at the heterointerfaces of Nb_2O_5 and TiO_2 .

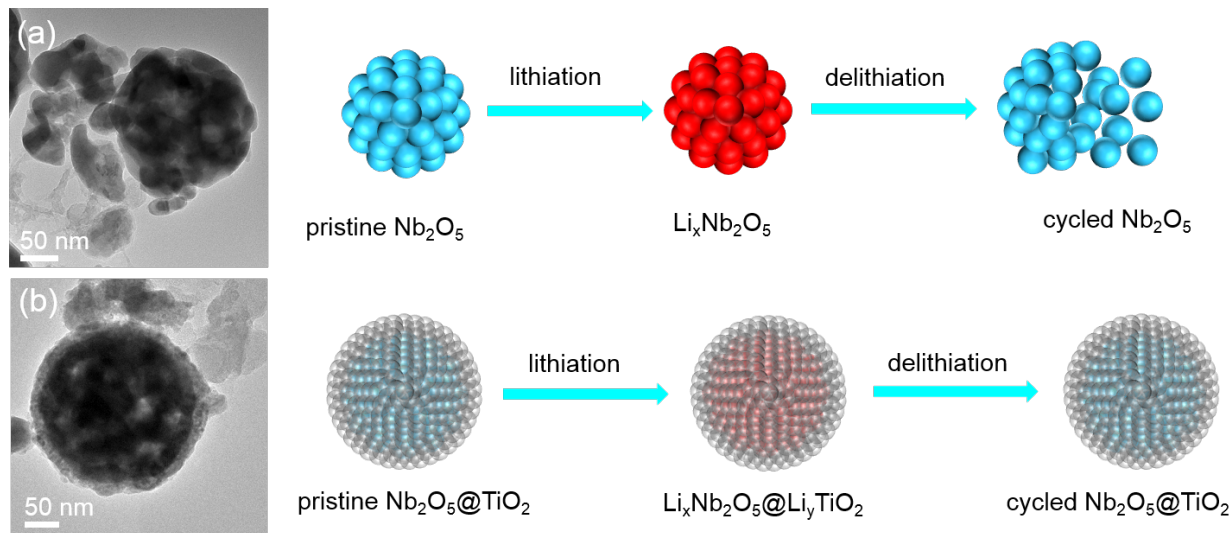


Figure 5. TEM images of (a) Nb_2O_5 and (b) $\text{Nb}_2\text{O}_5@\text{TiO}_2\text{c-13}$ after 1000 cycles at 0.5 A g^{-1} and their structural evolution scheme during de-/lithiation processes.

TEM was employed to investigate the morphologies of Nb_2O_5 , anatase TiO_2 , and $\text{Nb}_2\text{O}_5@\text{TiO}_2\text{c-13}$ after 1000 cycles at 0.5 A g^{-1} . As shown in **Figure 5a**, it is observed that the spherical Nb_2O_5 is fractured, resulting from the volume expansion and contraction during cycling. In contrast, anatase TiO_2 maintains its original morphology (**Figure S19**). It should be emphasized that $\text{Nb}_2\text{O}_5@\text{TiO}_2\text{c-13}$ retains the core-shell spherical structure without apparent structural deformation (**Figure 5b**), demonstrating that the anatase TiO_2 shell is stable and mechanically strong enough to tolerate volume expansion/contraction of the Nb_2O_5 core upon repetitive lithium insertion and extraction. Moreover, to check the crystallinity of the $\text{Nb}_2\text{O}_5@\text{TiO}_2\text{c-13}$ electrode after cycling, XRD analysis of the cycled electrode was performed. As shown in **Figure S20**, The diffraction intensity of the cycled $\text{Nb}_2\text{O}_5@\text{TiO}_2\text{c-13}$ electrode is slightly reduced, indicating that the crystallinity slightly reduces upon cycling.

On the account of the above results and analyses, the core-shell heterostructure plays the key role in enhancing the rate capability and cycling stability, which can facilitate charge transport and

enhance the surface reaction kinetics, as demonstrated in previous works.^{37, 39, 40, 45} Furthermore, the anatase TiO₂ shell acts as a protective layer for the Nb₂O₅ core, providing it with greater resistance to the volume changes it suffers during the lithiation/de-lithiation process, therefore, resulting in remarkably enhanced cycling performance.^{47, 49} Comparing the heterostructured Nb₂O₅@TiO₂ with single-phase titanium niobium oxides, the core-shell structure can not only effectively improve the intrinsically poor conductivity of the inner core and, thereby, improve rate capability, but also alleviate the mechanical stress generated in Nb₂O₅ during cycling, and thus increase the structural integrity. The mesoporous structure is another essential factor for the superior electrochemical behavior, as it possess abundant mesopores, which not only provides more accessible sites for Li-ion storage, but also facilitates the Li-ion diffusion.^{32, 40}

3. CONCLUSION

In summary, we have successfully synthesized mesoporous Nb₂O₅@TiO₂ core-shell heterostructures by a facile and reproducible sol-gel approach, and measured their electrochemical performance as electrode materials for LIBs. The results show that the lithium storage efficiency and stability strongly depend on the thickness of the anatase TiO₂ shell layer and the Nb₂O₅ spheres with 13 nm anatase TiO₂ coating layer achieve the best performance. Owing to the synergistic effects of the heterojunction and core-shell structure, the optimized material achieves higher electrochemical performance as compared to Nb₂O₅ and anatase TiO₂, with a high reversible capacity (206 mAh g⁻¹ at 0.1 A g⁻¹), superior rate capability (132 mAh g⁻¹ at 5 A g⁻¹), and excellent cycling stability (88.3% capacity retention after 1000 cycles). Such improvements emphasize the importance of the heterostructure in modifying the electrochemical behavior, which is helpful for designing battery materials with high performance.

4. EXPERIMENTAL METHODS

Materials: Titanium(IV) butoxide (97%, TBOT), cobalt(II) acetylacetone (97%), and acetophenone (99%) were purchased from Sigma Aldrich. Niobium(V) chloride was purchased from ABCR.

Synthesis of Nb₂O₅ spheres: Nb₂O₅ was synthesized by dissolving each niobium chloride (0.5 mmol) and cobalt(II) acetylacetone (0.5 mmol) in acetophenone (10 mL). Afterwards, the two solutions were mixed together. After being stirred for 24 h under argon, the solution was

transferred into a stainless-steel autoclave with a Teflon liner, and carefully sealed. The autoclave was heated in an oven at 220 °C for 6 h. The products were collected by centrifugation, thoroughly washed with acetone and ethanol, and dried at 70 °C in air. Subsequently, the product was calcined at 600 °C for 2 h in air.

Synthesis of anatase TiO₂: Anatase TiO₂ was synthesized by dissolving 0.3 mL TBOT in 10 mL ethanol, then the solution was added dropwise into a mixture of water and ethanol with a volume ratio of 1:20 under vigorous stirring. After 3 h of stirring, the products were collected by centrifugation, thoroughly washed with ethanol, and dried at 70 °C in air. Subsequently, the product was calcined at 400 °C for 1 h in air.

Synthesis of Nb₂O₅ spheres coated with TiO₂: For preparing the Nb₂O₅@TiO₂ with an anatase TiO₂ layer thickness of 13 nm, 45 μL TBOT was dissolved in 6 mL ethanol. 30 mg of Nb₂O₅ spheres was dissolved in a mixture solution of 0.6 mL water and 12 mL ethanol, to which the TBOT solution was added dropwise under vigorous stirring. After being stirred for 3 h, the products were collected by centrifugation, thoroughly washed with ethanol, and dried at 70 °C in air, denoted as Nb₂O₅@TiO₂a-14. Subsequently, the product was calcined at 400 °C for 1 h in air, denoted as Nb₂O₅@TiO₂c-13. Samples with other thickness of anatase TiO₂ (5 nm, 8 nm, and 22 nm) were prepared by following the same procedure, just varying the concentration of TBOT (15 μL, 30 μL, and 60 μL, respectively). The samples are denoted as Nb₂O₅@TiO₂c-5, Nb₂O₅@TiO₂c-8, and Nb₂O₅@TiO₂c-22 for anatase TiO₂ thicknesses of 5, 8, and 22 nm, respectively.

Characterizations: XRD patterns were recorded with a STOE MP diffractometer in transmission configuration using Mo Kα radiation ($\lambda=0.70930 \text{ \AA}$). Transmission electron microscopy (TEM) and high resolution TEM (HRTEM) images were obtained on a Philips CM 200 and FEI Talos 200S microscope operated at 200 kV. Raman spectra were obtained on a DXR Raman spectrometer (Thermo Scientific) with a 532 nm laser for illumination. The scattered light from the sample was dispersed by a 1200 lines/mm grating and collected by an Olympus microscope with a 100X objective. All X-ray photoelectron spectroscopy (XPS) measurements shown in the main manuscript were performed in an ultrahigh vacuum setup with a base pressure of $3\times10^{-10} \text{ mbar}$, employing the K_α radiation of a non-monochromated Mg X-ray source ($h\nu = 1253.6 \text{ eV}$) for excitation and an Omicron EA 125 hemispherical analyzer with a pass energy of 50 (20) eV for the survey (detail) scans to detect the kinetic energy of the emitted electrons. Additional

measurements shown in the Supporting Information were recorded at the ENERGIZE endstation at the Bessy II synchrotron facility, in an ultrahigh vacuum setup with a base pressure of 2×10^{-10} mbar, employing the K_{α} radiation of a non-monochromated Al X-ray source ($h\nu = 1486.6$ eV) for excitation and an ScientaOmicron DA30L hemispherical analyzer with a pass energy of 100 (50) eV for the survey (detail) scans. The powders were evenly distributed on carbon tape and measured without further treatment. The C1s peak of the carbon tape was set to 285.0 eV as a binding energy reference. Nitrogen sorption isotherms at -196°C were acquired on a Micromeritics ASAP 2020, after degassing the solids at 180°C overnight.

Electrochemical measurements: Electrochemical properties of active materials (anatase TiO_2 , Nb_2O_5 , $\text{Nb}_2\text{O}_5@\text{TiO}_2\text{c-5}$, $\text{Nb}_2\text{O}_5@\text{TiO}_2\text{c-8}$, $\text{Nb}_2\text{O}_5@\text{TiO}_2\text{c-13}$, and $\text{Nb}_2\text{O}_5@\text{TiO}_2\text{c-22}$) were evaluated by using CR2032-type coin cells, which were assembled in an Ar-filled glovebox. First, 70% active materials, 20% conductive carbon black (Super P, Timcal) and 10% polyvinylidene fluoride (PVDF, Alfa Aesar) were homogeneously mixed with N-methyl-2-pyrrolidone (NMP, anhydrous 99.5 %, Sigma-Aldrich). The resulting slurry was uniformly cast on Cu foil (Goodfellow, UK) with a doctor blade apparatus and then dried in a vacuum oven at 60°C for 1 hour. After a cold-laminating step, electrodes with a diameter of 12 mm were punched out and dried overnight at 120°C under vacuum using a Büchi glass oven. The mass loading of the active material is $\approx 1.5 \text{ mg cm}^{-2}$. Lithium metal foil was used as both counter and reference electrodes. 1 M LiPF_6 (ABCR, 99.9% battery grade) solution in a mixture of ethylene carbonate (EC, 99.9 %, ABCR), diethyl carbonate (DEC, 99.9%, ABCR) and dimethyl carbonate (DMC, 99.9%, ABCR) with 1:1:1 volume ratio was used as the electrolyte. A glass microfiber filter (Whatman) was used as a separator.

Galvanostatic charge-discharge cycling was carried out at room temperature using a CT2001 A battery testing system (Landt Instruments). Cyclic voltammograms (CVs) were measured on a Bio-Logic VMP3 multichannel potentiostat/galvanostat with a built-in electrochemical impedance spectroscopy (EIS) analyzer. EIS was tested at open-circuit potential (OCP), in the frequency range of 100 kHz to 0.1 Hz with an amplitude of 10 mV. Galvanostatic intermittent titration technique (GITT) analyses of $\text{Nb}_2\text{O}_5@\text{TiO}_2\text{c-13}$, Nb_2O_5 , and TiO_2 was performed at a current density of 20 mA g^{-1} , with a current pulse of 10 min followed with a relaxation step of 100 min. It should be

noted that, for electrochemical activation, the batteries were cycled for three cycles at a current density of 20 mA g⁻¹ (without pulses) before the GITT tests.

SUPPORTING INFORMATION

EDX spectra of Nb₂O₅. XPS spectra of Nb₂O₅, Nb₂O₅@TiO₂a-14, Nb₂O₅@TiO₂c-13, and anatase TiO₂. SEM and TEM images of Nb₂O₅, Nb₂O₅@TiO₂a-14, Nb₂O₅@TiO₂c-13, and anatase TiO₂. BET data of anatase TiO₂, Nb₂O₅, Nb₂O₅@TiO₂a-14, and Nb₂O₅@TiO₂c-13. TEM and HRTEM images of Nb₂O₅@TiO₂c-5, Nb₂O₅@TiO₂c-8, and Nb₂O₅@TiO₂c-22. The weight ratio between Nb₂O₅ and anatase TiO₂. XRD of Nb₂O₅@TiO₂c-5, Nb₂O₅@TiO₂c-8, and Nb₂O₅@TiO₂c-22. Electrochemical performances of Nb₂O₅@TiO₂c-5, Nb₂O₅@TiO₂c-8, and Nb₂O₅@TiO₂c-22 as anodes in Li-ion half cells. TEM images of Nb₂O₅@TiO₂c-5, Nb₂O₅@TiO₂c-8, and Nb₂O₅@TiO₂c-22 after cycling stability tests. The first two Galvanostatic discharge-charge curves of Nb₂O₅, TiO₂, and Nb₂O₅@TiO₂c-13 at 0.1 A g⁻¹. Galvanostatic charge and discharge curves of Nb₂O₅, TiO₂, and Nb₂O₅@TiO₂c-13 cycled at different cycles. Electrochemical performances of Nb₂O₅, TiO₂, and Nb₂O₅@TiO₂c-13 at a current density of 0.1 A g⁻¹. Electrochemical performances of Nb₂O₅@TiO₂c-14 as anodes in Li-ion half cells. CV curves of Nb₂O₅@TiO₂c-13, Nb₂O₅, and TiO₂. Capacitive-controlled contributions of Nb₂O₅@TiO₂c-13, Nb₂O₅, and TiO₂. Galvanostatic intermittent titration technique (GITT) curves of Nb₂O₅@TiO₂c-13, Nb₂O₅, and TiO₂. The calculated Li-ion diffusion coefficients from GITT. GITT voltage profile of a single current pulse-relaxation step. TEM image of anatase TiO₂ after 1000 cycles at 0.5 A g⁻¹. XRD of Nb₂O₅@TiO₂c-13 before and after 1000 cycles at 0.5 A g⁻¹.

AUTHOR INFORMATION

Corresponding Author

Nicola Pinna – Institut für Chemie and IRIS Adlershof, Humboldt-Universität zu Berlin, 12489 Berlin, Germany; orcid.org/0000-0003-1273-803X; E-mail: nicola.pinna@hu-berlin.de

Authors

Wenlei Xu – Institut für Chemie and IRIS Adlershof, Humboldt-Universität zu Berlin, 12489 Berlin, Germany; orcid.org/0000-0003-4226-1789

Yaolin Xu – Department of Electrochemical Energy Storage, Helmholtz-Zentrum Berlin für Materialien und Energie, 14109 Berlin, Germany; orcid.org/0000-0002-2658-3852

Yan Lu – Department of Electrochemical Energy Storage, Helmholtz-Zentrum Berlin für Materialien und Energie, 14109 Berlin, Germany; orcid.org/0000-0003-3055-0073

Thorsten Schultz – Institut für Physik and IRIS Adlershof, Humboldt-Universität zu Berlin, 12489 Berlin, Germany; Helmholtz-Zentrum Berlin für Materialien und Energie GmbH, 12489 Berlin, Germany; orcid.org/0000-0002-0344-6302

Norbert Koch – Institut für Physik and IRIS Adlershof, Humboldt-Universität zu Berlin, 12489 Berlin, Germany; Helmholtz-Zentrum Berlin für Materialien und Energie GmbH, 12489 Berlin, Germany; orcid.org/0000-0002-6042-6447

Notes

The authors declare no competing financial interest.

ACKNOWLEDGEMENTS

W. X. acknowledges the fellowship from the China Scholarship Council (CSC). Christoph Erdmann and Xuefeng Pan are acknowledged for TEM and SEM measurements, respectively. Chengxu Shen is acknowledged for Raman measurement, Yu Wang and Wei Zhang are acknowledged for fruitful discussions.

REFERENCES

1. Etacheri, V.; Marom, R.; Elazari, R.; Salitra, G.; Aurbach, D. Challenges in the development of advanced Li-ion batteries: a review. *Energy Environ. Sci.* **2011**, 4 (9), 3243-3262.
2. Li, M.; Lu, J.; Chen, Z.; Amine, K. 30 Years of Lithium-Ion Batteries. *Adv. Mater.* **2018**, 30 (33), 1800561.
3. Noori, A.; El-Kady, M. F.; Rahmanifar, M. S.; Kaner, R. B.; Mousavi, M. F. Towards establishing standard performance metrics for batteries, supercapacitors and beyond. *Chem. Soc. Rev.* **2019**, 48 (5), 1272-1341.
4. Shen, F.; Sun, Z.; He, Q.; Sun, J.; Kaner, R. B.; Shao, Y. Niobium pentoxide based materials for high rate rechargeable electrochemical energy storage. *Mater. Horiz.* **2021**, 8 (4), 1130-1152.
5. Han, X.; Russo, P. A.; Goubard-Bretesché, N.; Patanè, S.; Santangelo, S.; Zhang, R.; Pinna, N., Exploiting the Condensation Reactions of Acetophenone to Engineer Carbon-Encapsulated Nb₂O₅ Nanocrystals for High-Performance Li and Na Energy Storage Systems. *Adv. Energy Mater.* **2019**, 9 (42), 1902813.
6. Yi, T.-F.; Sari, H. M. K.; Li, X.; Wang, F.; Zhu, Y.-R.; Hu, J.; Zhang, J.; Li, X., A review of niobium oxides based nanocomposites for lithium-ion batteries, sodium-ion batteries and supercapacitors. *Nano Energy* **2021**, 85, 105955.

7. Augustyn, V.; Come, J.; Lowe, M. A.; Kim, J. W.; Taberna, P.-L.; Tolbert, S. H.; Abruña, H. D.; Simon, P.; Dunn, B. High-rate electrochemical energy storage through Li⁺ intercalation pseudocapacitance. *Nat. Mater.* **2013**, 12 (6), 518-522.
8. Chen, D.; Wang, J.-H.; Chou, T.-F.; Zhao, B.; El-Sayed, M. A.; Liu, M. Unraveling the Nature of Anomalously Fast Energy Storage in T-Nb₂O₅. *J. Am. Chem. Soc.* **2017**, 139 (20), 7071-7081.
9. Griffith, K. J.; Forse, A. C.; Griffin, J. M.; Grey, C. P. High-Rate Intercalation without Nanostructuring in Metastable Nb₂O₅ Bronze Phases. *J. Am. Chem. Soc.* **2016**, 138 (28), 8888-8899.
10. Li, H.; Zhu, Y.; Dong, S.; Shen, L.; Chen, Z.; Zhang, X.; Yu, G. Self-Assembled Nb₂O₅ Nanosheets for High Energy–High Power Sodium Ion Capacitors. *Chem. Mater.* **2016**, 28 (16), 5753-5760.
11. Liu, M.; Yan, C.; Zhang, Y. Fabrication of Nb₂O₅ Nanosheets for High-rate Lithium Ion Storage Applications. *Sci. Rep.* **2015**, 5 (1), 8326.
12. Deng, B.; Lei, T.; Zhu, W.; Xiao, L.; Liu, J. In-Plane Assembled Orthorhombic Nb₂O₅ Nanorod Films with High-Rate Li⁺ Intercalation for High-Performance Flexible Li-Ion Capacitors. *Adv. Funct. Mater.* **2018**, 28 (1), 1704330.
13. Yang, H.; Xu, H.; Wang, L.; Zhang, L.; Huang, Y.; Hu, X. Microwave-Assisted Rapid Synthesis of Self-Assembled T-Nb₂O₅ Nanowires for High-Energy Hybrid Supercapacitors. *Chem. Eur. J.* **2017**, 23 (17), 4203-4209.
14. Song, H.; Fu, J.; Ding, K.; Huang, C.; Wu, K.; Zhang, X.; Gao, B.; Huo, K.; Peng, X.; Chu, P. K. Flexible Nb₂O₅ nanowires/graphene film electrode for high-performance hybrid Li-ion supercapacitors. *J. Power Sources* **2016**, 328, 599-606.
15. Huang, C.; Fu, J.; Song, H.; Li, X.; Peng, X.; Gao, B.; Zhang, X.; Chu, P. K. General fabrication of mesoporous Nb₂O₅ nanobelts for lithium ion battery anodes. *RSC Adv.* **2016**, 6 (93), 90489-90493.
16. Cheong, J. Y.; Jung, J.-W.; Youn, D.-Y.; Kim, C.; Yu, S.; Cho, S.-H.; Yoon, K. R.; Kim, I.-D. Mesoporous orthorhombic Nb₂O₅ nanofibers as pseudocapacitive electrodes with ultra-stable Li storage characteristics. *J. Power Sources* **2017**, 360, 434-442.
17. Meng, J.; He, Q.; Xu, L.; Zhang, X.; Liu, F.; Wang, X.; Li, Q.; Xu, X.; Zhang, G.; Niu, C.; Xiao, Z.; Liu, Z.; Zhu, Z.; Zhao, Y.; Mai, L. Identification of Phase Control of Carbon-Confining Nb₂O₅ Nanoparticles toward High-Performance Lithium Storage. *Adv. Energy Mater.* **2019**, 9 (18), 1802695.
18. Zhao, Y.; Zhou, X.; Ye, L.; Chi Edman Tsang, S. Nanostructured Nb₂O₅ catalysts. *Nano Rev.* **2012**, 3 (1), 17631.
19. Jiang, H.; Yang, L.; Li, C.; Yan, C.; Lee, P. S.; Ma, J. High-rate electrochemical capacitors from highly graphitic carbon-tipped manganese oxide/mesoporous carbon/manganese oxide hybrid nanowires. *Energy Environ. Sci.* **2011**, 4 (5), 1813-1819.
20. Qu, K.; Wang, Y.; Vasileff, A.; Jiao, Y.; Chen, H.; Zheng, Y., Polydopamine-inspired nanomaterials for energy conversion and storage. *J. Mater. Chem. A* **2018**, 6 (44), 21827-21846.
21. Han, X.; Russo, P. A.; Triolo, C.; Santangelo, S.; Goubard-Bretesché, N.; Pinna, N. Comparing the Performance of Nb₂O₅ Composites with Reduced Graphene Oxide and Amorphous Carbon in Li- and Na-Ion Electrochemical Storage Devices. *ChemElectroChem* **2020**, 7 (7), 1689-1698.

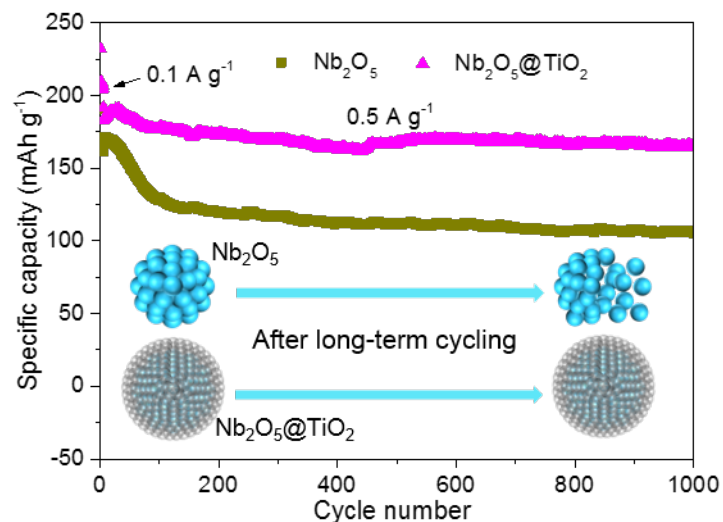
22. AbdelHamid, A. A.; Mendoza-Garcia, A.; Ying, J. Y. Advances in and prospects of nanomaterials' morphological control for lithium rechargeable batteries. *Nano Energy*, **2022**, 93, 106860.
23. Ali, Y.; Iqbal, N.; Lee, S. Role of SEI layer growth in fracture probability in lithium-ion battery electrodes. *Int. J. Energy Res.* **2021**, 45, 5293-5308.
24. Yang, Y.; Zhu, H.; Xiao, J.; Geng, H.; Zhang, Y.; Zhao, J.; Li, G.; Wang, X.-L.; Li, C. C.; Liu, Q. Achieving Ultrahigh-Rate and High-Safety Li⁺ Storage Based on Interconnected Tunnel Structure in Micro-Size Niobium Tungsten Oxides. *Adv.Mater.* **2020**, 32 (12), 1905295.
25. Song, Z.; Li, H.; Liu, W.; Zhang, H.; Yan, J.; Tang, Y.; Huang, J.; Zhang, H.; Li, X. Ultrafast and Stable Li-(De)intercalation in a Large Single Crystal H-Nb₂O₅ Anode via Optimizing the Homogeneity of Electron and Ion Transport. *Adv. Mater.* **2020**, 32 (22), 2001001.
26. Li, W.; Liu, J.; Zhao, D. Mesoporous materials for energy conversion and storage devices. *Nat. Rev. Mater.* **2016**, 1 (6), 16023.
27. Qiu, P.; Ma, B.; Hung, C. T.; Li, W.; Zhao, D. Spherical mesoporous materials from single to multilevel architectures. *Acc. Chem. Res.* 52 (10), 2928-2938.
28. Zheng, X., Shen, G., Wang, C.; Li, Y.; Dunphy, D.; Hasan, T.; Brinker, C. J.; Su, B.-L. Bio-inspired Murray materials for mass transfer and activity. *Nat. Commun.* **2017**, 8, 14921.
29. Lou, L.; Kong, X.; Zhu, T.; Lin, J. Liang, S.; Liu, F.; Cao, G.; Pan, A. Facile fabrication of interconnected-mesoporous T-Nb₂O₅ nanofibers as anodes for lithium-ion batteries. *Sci. China Mater.* **2019**, 62, 465-473.
30. Kim, H.; Lim, E.; Jo, C.; Yoon, G.; Hwang, J.; Jeong, S.; Lee. J.; Kang, K. Ordered-mesoporous Nb₂O₅/carbon composite as a sodium insertion material. *Nano Energy* **2015**, 16, 62-70.
31. Lim, E.; Kim, H.; Jo, C.; Chun, J.; Ku, K.; Kim, S.; Lee, H. I.; Nam, I.-S.; Yoon, S.; Kang, K.; Lee, J. Advanced Hybrid Supercapacitor Based on a Mesoporous Niobium Pentoxide/Carbon as High-Performance Anode. *ACS Nano* **2014**, 8 (9), 8968-8978.
32. Wang, L.; Bi, X.; Yang, S. Partially Single-Crystalline Mesoporous Nb₂O₅ Nanosheets in between Graphene for Ultrafast Sodium Storage. *Adv. Mater.* **2016**, 28, 7672-7679.
33. Yoo, Y.; Kang, Y. C. Mesoporous Nb₂O₅ microspheres with filled and yolk-shell structure as anode materials for lithium-ion batteries. *J. Alloys Compd.* **2019**, 776, 722-730.
34. Liu, G.; Jin, B.; Bao, K.; Xie, H.; Guo, J.; Ji, X.; Zhang, R.; Jiang, Q. Facile synthesis of porous Nb₂O₅ microspheres as anodes for lithium-ion batteries. *Int. J. Hydrog. Energy* **2017**, 42 (19), 6065-6071.
35. Nasrin, K.; Sudharshan, V.; Subramani, K.; Karnan, M.; Sathish, M. In-Situ Synergistic 2D/2D MXene/BCN Heterostructure for Superlative Energy Density Supercapacitor with Super-Long Life. *Small* **2022**, 18 (4), 2106051.
36. Chen, C.; Xie, X.; Anasori, B.; Sarycheva, A.; Makaryan, T.; Zhao, M.; Urbankowski, P.; Miao, L.; Jiang, J.; Gogotsi, Y. MoS₂-on-MXene Heterostructures as Highly Reversible Anode Materials for Lithium-Ion Batteries. *Angew.Chem.Int.Ed.* **2018**, 57 (7), 1846-1850.
37. Zheng, Y.; Zhou, T.; Zhang, C.; Mao, J.; Liu, H.; Guo, Z. Boosted Charge Transfer in SnS/SnO₂ Heterostructures: Toward High Rate Capability for Sodium-Ion Batteries. *Angew.Chem.Int.Ed.* **2016**, 55 (10), 3408-3413.

38. Lee, G.; Kim, S.; Kim, S.; Choi, J. SiO₂/TiO₂ Composite Film for High Capacity and Excellent Cycling Stability in Lithium-Ion Battery Anodes. *Adv. Funct. Mater.* **2017**, 27 (39), 1703538.
39. Wang, T.; Legut, D.; Fan, Y.; Qin, J.; Li, X.; Zhang, Q. Building Fast Diffusion Channel by Constructing Metal Sulfide/Metal Selenide Heterostructures for High-Performance Sodium Ion Batteries Anode. *Nano Lett.* **2020**, 20 (8), 6199-6205.
40. Khatoon, R.; Guo, Y.; Attique, S.; Khan, K.; Treen, A. K.; Haq, M. U.; Tang, H.; Chen, H.; Tian, Y.; Nisar, M.; Din, S. U.; Lu, J. Facile synthesis of α -Fe₂O₃/Nb₂O₅ heterostructure for advanced Li-Ion batteries. *J. Alloys Compd.* **2020**, 837, 155294.
41. Fang, Y., Lv, Y., Gong, F., Elzatahry, A.A., Zheng, G. and Zhao, D. Synthesis of 2D-Mesoporous-Carbon/MoS₂ Heterostructures with Well-Defined Interfaces for High-Performance Lithium-Ion Batteries. *Adv. Mater.* **2016**, 28, 9385-9390.
42. Lim, E.; Jo, C.; Kim, H.; Kim, M.-H.; Mun, Y.; Chun, J.; Ye, Y.; Hwang, J.; Ha, K.-S.; Roh, K. C.; Kang, K.; Yoon, S.; Lee, J. Facile Synthesis of Nb₂O₅@Carbon Core–Shell Nanocrystals with Controlled Crystalline Structure for High-Power Anodes in Hybrid Supercapacitors. *ACS Nano*, **2015**, 9 (7), 7497-7505.
43. Xing, L.; Yu, Q.; Jiang, B.; Chu, J.; Lao, C.-Y.; Wang, M.; Han, K.; Liu, Z.; Bao, Y.; Wang, W. Carbon-encapsulated ultrathin MoS₂ nanosheets epitaxially grown on porous metallic TiNb₂O₆ microspheres with unsaturated oxygen atoms for superior potassium storage. *J. Mater. Chem. A* **2019**, 7 (10), 5760-5768.
44. Balogun, M.-S.; Qiu, W.; Luo, Y.; Meng, H.; Mai, W.; Onasanya, A.; Olaniyi, T. K.; Tong, Y. A review of the development of full cell lithium-ion batteries: The impact of nanostructured anode materials. *Nano Res.* **2016**, 9 (10), 2823-2851.
45. Huang, H.; Zhao, G.; Sun, X.; Yu, X.; Liu, C.; Shen, X.; Wang, M.; Lyu, P.; Zhang, N. Built-in electric field enhanced ionic transport kinetics in the T-Nb₂O₅@MoO₂ heterostructure. *J. Mater. Chem. A* **2021**, 9 (40), 22854-22860.
46. Zhou, T.; Zheng, Y.; Gao, H.; Min, S.; Li, S.; Liu, H. K.; Guo, Z. Surface Engineering and Design Strategy for Surface-Amorphized TiO₂@Graphene Hybrids for High Power Li-Ion Battery Electrodes. *Adv. Sci.* **2015**, 2 (9), 1500027.
47. Yang, J.; Wang, Y.; Li, W.; Wang, L.; Fan, Y.; Jiang, W.; Luo, W.; Wang, Y.; Kong, B.; Selomulya, C.; Liu, H. K.; Dou, S. X.; Zhao, D. Amorphous TiO₂ Shells: A Vital Elastic Buffering Layer on Silicon Nanoparticles for High-Performance and Safe Lithium Storage. *Adv. Mater.* **2017**, 29 (48), 1700523.
48. Wang, H.; Ma, D.; Huang, X.; Huang, Y.; Zhang, X. General and Controllable Synthesis Strategy of Metal Oxide/TiO₂ Hierarchical Heterostructures with Improved Lithium-Ion Battery Performance. *Sci. Rep.* **2012**, 2 (1), 701.
49. Ren, W.; Zhou, W.; Zhang, H.; Cheng, C. ALD TiO₂-Coated Flower-like MoS₂ Nanosheets on Carbon Cloth as Sodium Ion Battery Anode with Enhanced Cycling Stability and Rate Capability. *ACS Appl. Mater. Interfaces* **2017**, 9 (1), 487-495.
50. Zhang, L.; Gu, X.; Yan, C.; Zhang, S.; Li, L.; Jin, Y.; Zhao, S.; Wang, H.; Zhao, X. Titanosilicate Derived SiO₂/TiO₂@C Nanosheets with Highly Distributed TiO₂ Nanoparticles in SiO₂ Matrix as Robust Lithium Ion Battery Anode. *ACS Appl. Mater. Interfaces* **2018**, 10 (51), 44463-44471.
51. Yu, L.; Wang, Z.; Zhang, L.; Wu, H. B.; Lou, X. W. TiO₂ nanotube arrays grafted with Fe₂O₃ hollow nanorods as integrated electrodes for lithium-ion batteries. *J. Mater. Chem. A* **2013**, 1 (1), 122-127.

52. Guo, B.; Yu, X.; Sun, X.-G.; Chi, M.; Qiao, Z.-A.; Liu, J.; Hu, Y.-S.; Yang, X.-Q.; Goodenough, J. B.; Dai, S. A long-life lithium-ion battery with a highly porous $TiNb_2O_7$ anode for large-scale electrical energy storage. *Energy Environ. Sci.* **2014**, *7* (7), 2220-2226.
53. Cheng, Q.; Liang, J.; Zhu, Y.; Si, L.; Guo, C.; Qian, Y. Bulk $Ti_2Nb_{10}O_{29}$ as long-life and high-power Li-ion battery anodes. *J. Mater. Chem. A* **2014**, *2* (41), 17258-17262.
54. Griffith, K. J.; Harada, Y.; Egusa, S.; Ribas, R. M.; Monteiro, R. S.; Von Dreele, R. B.; Cheetham, A. K.; Cava, R. J.; Grey, C. P.; Goodenough, J. B. Titanium Niobium Oxide: From Discovery to Application in Fast-Charging Lithium-Ion Batteries. *Chem. Mater.* **2021**, *33* (1), 4-18.
55. Liu, Y.; Lin, L.; Zhang, W.; Wei, M. Heterogeneous $TiO_2@Nb_2O_5$ composite as a high-performance anode for lithium-ion batteries. *Sci. Rep.* **2017**, *7*, 7204.
56. Yu, X.; Xin, L.; Liu, Y.; Zhao, W.; Li, B.; Zhou, X.; Shen, H. One-step synthesis of Nb-doped TiO_2 rod@ Nb_2O_5 nanosheet core-shell heterostructures for stable high-performance lithium-ion batteries. *RSC Adv.* **2016**, *6*, 27094-27101.
57. Mokhlesur Rahman, M.; Zhou, M.; Sultana, I.; Mateti, S.; Falin, A.; Li, L.; Wu, Z.; Chen, Y. *Batteries & Supercaps* **2019**, *2*, 160.
58. Skroczky, K.; Antunes, M. M.; Han, X.; Santangelo, S.; Scholz, G.; Valente, A. A.; Pinna, N.; Russo, P. A. Niobium pentoxide nanomaterials with distorted structures as efficient acid catalysts. *Commun. Chem.* **2019**, *2* (1), 129.
59. Han, X.; Wahl, S.; Russo, P. A.; Pinna, N. Cobalt-Assisted Morphology and Assembly Control of Co-Doped ZnO Nanoparticles. *Nanomaterials* **2018**, *8* (4), 249.
60. Choi, H. C.; Jung, Y. M.; Kim, S. B. Size effects in the Raman spectra of TiO_2 nanoparticles. *Vib. Spectrosc.* **2005**, *37* (1), 33-38.
61. Gardecka, A. J.; Goh, G. K. L.; Sankar, G.; Parkin, I. P. On the nature of niobium substitution in niobium doped titania thin films by AACVD and its impact on electrical and optical properties. *J. Mater. Chem. A* **2015**, *3* (34), 17755-17762.
62. Netterfield, R. P.; Martin, P. J.; Pacey, C. G.; Sainty, W. G.; McKenzie, D. R.; Auchterlonie, G. Ion-assisted deposition of mixed TiO_2 - SiO_2 films. *J. Appl. Phys.* **1989**, *66* (4), 1805-1809.
63. Deng, Q.; Chen, F.; Liu, S.; Bayaguud, A.; Feng, Y.; Zhang, Z.; Fu, Y.; Yu, Y.; Zhu, C. Advantageous Functional Integration of Adsorption-Intercalation-Conversion Hybrid Mechanisms in 3D Flexible $Nb_2O_5@$ Hard Carbon@ $MoS_2@$ Soft Carbon Fiber Paper Anodes for Ultrafast and Super-Stable Sodium Storage. *Adv. Funct. Mater.* **2020**, *30* (10), 1908665.
64. Hao, Z.; Chen, Q.; Dai, W.; Ren, Y.; Zhou, Y.; Yang, J.; Xie, S.; Shen, Y.; Wu, J.; Chen, W.; Xu, G. Q. Oxygen-Deficient Blue TiO_2 for Ultrastable and Fast Lithium Storage. *Adv. Energy Mater.* **2020**, *10* (10), 1903107.
65. Jiang, J.; Zhu, J.; Ai, W.; Fan, Z.; Shen, X.; Zou, C.; Liu, J.; Zhang, H.; Yu, T. Evolution of disposable bamboo chopsticks into uniform carbon fibers: a smart strategy to fabricate sustainable anodes for Li-ion batteries. *Energy Environ. Sci.* **2014**, *7*, 2670-2679.
66. Ai, W.; Jiang, J.; Zhu, J.; Fan, Z.; Wang, Y.; Zhang, H.; Huang, W.; Yu, T. Supramolecular Polymerization Promoted In Situ Fabrication of Nitrogen-Doped Porous Graphene Sheets as Anode Materials for Li-Ion Batteries. *Adv. Energy Mater.* **2015**, *5* (15), 1500559.

67. Xu, W.; Russo, P. A.; Schultz, T.; Koch, N.; Pinna, N., Niobium-Doped Titanium Dioxide with High Dopant Contents for Enhanced Lithium-Ion Storage. *ChemElectroChem* **2020**, 7 (19), 4016-4023.
68. Shin, J.-Y., Samuelis, D. and Maier, J. Sustained Lithium-Storage Performance of Hierarchical, Nanoporous Anatase TiO₂ at High Rates: Emphasis on Interfacial Storage Phenomena. *Adv. Funct. Mater.* **2011**, 21 (18), 3464-3472.
69. Lu, X.; Jian, Z.; Fang, Z.; Gu, L.; Hu, Y.-S.; Chen, W.; Wang, Z.; Chen, L. Atomic-scale investigation on lithium storage mechanism in TiNb₂O₇. *Energy Environ. Sci.* **2011**, 4 (8), 2638-2644.
70. Huang, S.; Zhang, L.; Liu, L.; Liu, L.; Li, J.; Hu, H.; Wang, J.; Ding, F.; Schmidt, O. G. Rationally engineered amorphous TiO_x/Si/TiO_x nanomembrane as an anode material for high energy lithium ion battery. *Energy Stor. Mater.* **2018**, 12, 23-29.
71. Xu, H.; Li, S.; Zhang, C.; Chen, X.; Liu, W.; Zheng, Y.; Xie, Y.; Huang, Y.; Li, J. Roll-to-roll prelithiation of Sn foil anode suppresses gassing and enables stable full-cell cycling of lithium ion batteries. *Energy Environ. Sci.* **2019**, 12 (10), 2991-3000.
72. Feng, T.; Xu, Y.; Zhang, Z.; Du, X.; Sun, X.; Xiong, L.; Rodriguez, R.; Holze, R. Low-Cost Al₂O₃ Coating Layer As a Preformed SEI on Natural Graphite Powder To Improve Coulombic Efficiency and High-Rate Cycling Stability of Lithium-Ion Batteries. *ACS Appl. Mater. Interfaces* **2016**, 8 (10), 6512-6519.
73. Shih, W. S.; Young, S. J.; Ji, L. W.; Water, W.; Shiu, H. W. TiO₂-Based Thin Film Transistors with Amorphous and Anatase Channel Layer. *J. Electrochem. Soc.* **2011**, 158, H609.
74. Yuwono, J. A.; Burr, P.; Galvin C.; Lennon, A. Atomistic Insights into Lithium Storage Mechanisms in Anatase, Rutile, and Amorphous TiO₂ Electrodes. *ACS Appl. Mater. Interfaces* **2021**, 13 (1), 1791-1806.
75. Zheng, Y.; Yao, Z.; Shadike, Z.; Lei, M.; Liu, J.; Li, C. Defect-Concentration-Mediated T-Nb₂O₅ Anodes for Durable and Fast-Charging Li-Ion Batteries. *Adv. Funct. Mater.* **2022**, 32 (12), 2107060.
76. Brezesinski, T.; Wang, J.; Tolbert, S. H.; Dunn, B. Ordered mesoporous α -MoO₃ with iso-oriented nanocrystalline walls for thin-film pseudocapacitors. *Nat. Mater.* **2010**, 9 (2), 146-151.

Table of Contents graphic



Heterostructured mesoporous $\text{Nb}_2\text{O}_5@\text{TiO}_2$ core-shell spheres have been synthesized by a facile sol-gel method. The synergistic effect of the heterojunction and core-shell structure is investigated for a high-performance anode in lithium-ion batteries (LIBs). By controlling the thickness of TiO_2 shell layer, the heterostructured material exhibits superior electrochemical performance as compared to pure Nb_2O_5 and anatase TiO_2 , due to the improved electronic conductivity and structural stability.